

Stellar Parameters and Chemical Abundances of G Giants

Liang WANG

Key Laboratory of Optical Astronomy, National Astronomical Observatories, Chinese Academy of Sciences, A20, Datun Road, Chaoyang District, Beijing 100012, China

Graduate University of the Chinese Academy of Sciences, 19A Yuquan Road, Shijingshan District, Beijing 100049, China

wangliang@nao.cas.cn

Yujuan LIU

Key Laboratory of Optical Astronomy, National Astronomical Observatories, Chinese Academy of Sciences, A20, Datun Road, Chaoyang District, Beijing 100012, China

lyj@nao.cas.cn

Gang ZHAO

Key Laboratory of Optical Astronomy, National Astronomical Observatories, Chinese Academy of Sciences, A20, Datun Road, Chaoyang District, Beijing 100012, China

gzhao@nao.cas.cn

and

Bun'ei SATO

Tokyo Institute of Technology, 2-12-1 Ookayama, Meguro-ku, Tokyo 152-8550, Japan

sato.b.aa@m.titech.ac.jp

(Received ; accepted)

Abstract

We present basic stellar parameters of 99 late-type G giants based on high resolution spectra obtained by the High Dispersion Spectrograph attached to Subaru Telescope. These stars are targets of a Doppler survey program searching for extra-solar planets among evolved stars, with a metallicity of $-0.8 < [\text{Fe}/\text{H}] < +0.2$. We also derived their abundances of 15 chemical elements, including four α -elements (Mg, Si, Ca, Ti), three odd-Z light elements (Al, K, Sc), four iron peak elements (V, Cr, Fe, Ni), and four neutron-capture elements (Y, Ba, La, Eu). Kinematic properties reveal that most of the program stars belong to the thin disk.

Key words: stars: abundances — stars: atmospheres — stars: fundamental parameters — stars: late-type

1. Introduction

Since the first extra-solar planet around main sequence star, 51 Peg b was discovered in 1995 (Mayor & Queloz 1995), more than 500 planets have been revealed in solar neighbourhood¹, providing clues on planet formation process around different types of stars. However, only a small fraction of known planet-host stars are intermediate-mass ($1.5 \sim 5M_{\odot}$). Properties of planets around these stars are of great importance to constrain planet formation theories (e.g. Ida & Lin 2004). One way to search for extra-solar planets around intermediate-mass stars is monitoring radial velocities of late-type G, K giants. Their spectra have many sharp absorption lines, and therefore suitable for getting precise radial velocity data by modern Doppler techniques (e.g. Butler et al. 1996).

The East Asian Planets Search Network (EAPSNet, see Izumiura 2005) which was started in 2005 has established an international consortium among Japanese, Korean and Chinese researchers. More than 500 late-type G, K giants are being monitored with 2-m class telescopes among three countries. Stellar parameters and detailed elemental abundances of some of the targets have been analysed by Tekeda et al. (2008) and Liu et al. (2010). As an extension of EAPSNet, the Subaru Planets Search Program started monitoring radial velocity variations of about 300 late-type G, K giants in 2006. By the end of June 2010, two planets (HD 145457b and HD 180314b) have been discovered in this program (Sato et al. 2010). While basic parameters and chemical abundance analysis have not been conducted for this sample.

In this paper we present the first results of stellar parameters and chemical abundances for 99 giants based on high resolution spectra obtained with Subaru Telescope. In Section 2, we describe the observation and data reduction method. Section 3 gives the derived stellar parameters, including the comparison of different methods. Chemical abundances and kinematic properties are presented in Section 4 and 5, respectively. In the last section, conclusions are presented.

2. Observation and data reduction

Targets of Subaru Planet Search Program were selected from *Hipparcos Catalogue* (ESA 1997) by the following criteria,

1. a colour index of $0.6 \lesssim B - V \lesssim 1.0$ and an absolute magnitude of $-3 \lesssim M_V \lesssim 2.5$, corresponding to the range of evolved, late-type G giants.
2. a magnitude of $6.5 < V < 7.0$, which enables follow-up observations using 2m-class telescopes.
3. a declination of $\delta > -25^{\circ}$ so as to be observable in Japan, Korea and China.

First, each target was observed with the High Dispersion Spectrograph (HDS; Noguchi et al.

¹ see <http://exoplanets.org/>

2002) equipped to Subaru Telescope three times with an interval of about 1.5 months, for the purpose of quickly identifying stars with large radial velocity variations. Then the most likely candidates with sub-stellar companions were repeatedly observed with the 1.88m telescope at Okayama Astrophysical Observatory (OAO, Japan), 1.8m telescope at Bohyunsan Optical Astronomy Observatory (BOAO, Korea), and 2.16m telescope at Xinglong Station (National Astronomical Observatories, China).

HDS has several setups of gratings, and each has different spectrum format and wavelength coverage. In the first three runs of this program in 2006, we used StdI2b twice and StdI2a once. The spectra taken with StdI2a setup with a wavelength coverage of 4900~7600 Å are suitable for chemical abundance analysis. Here we present the first results of these 99 stars whose spectra were obtained in July, 2006, with a resolving power of $R \sim 60,000$ and a typical signal-to-noise ratio (SNR) of 150-230/pixel. The bias is determined and subtracted using the over-scan region on CCD, with an IRAF script provided by HDS web page ². Then, the reduction of data follows the standard routines. The MIDAS/ECHELLE package is used for order definition, flat-fielding, background subtraction, 1-D spectra extraction, and wavelength calibration. The radial velocity shift is corrected by fitting profiles of about 80 pre-selected lines with intermediate strength. Although the Doppler shift correction is made on the unnormalized spectra, the spectra lines are narrow (typically ~ 0.3 Å) so that the continuum around such a line could be seen as a constant, and nearly do not affect the measured central wavelength. The uncertainties of radial velocity values are about $0.3 \sim 0.4 \text{ km s}^{-1}$ using this method (see table 8). After that, the one dimension spectra are normalized by a continuum fit by a cubic spline function with a smooth parameter. The spline interpolation is determined by a set of continuum windows selected from a typical giant spectrum, usually has a density of 10-15 points per order.

For the purpose of precise radial velocity measurement, the spectra were taken with an iodine vapor cell inserted into the light path of the spectrograph, hence the stellar spectral lines located in the wavelength of 5000~6300 Å region were heavily mixed with absorption features in the I₂ spectrum. We only use the red part of the spectra with wavelength longer than 6350 Å to analyse the chemical abundances. Equivalent widths are measured by fitting the line profiles with a Gaussian function for the weak lines. While in strong unblended lines, broad damping wings contribute significantly to the equivalent width. The direct integration is used for such kind of lines alternatively.

² see <http://www.naoj.org/Observing/Instruments/HDS/>

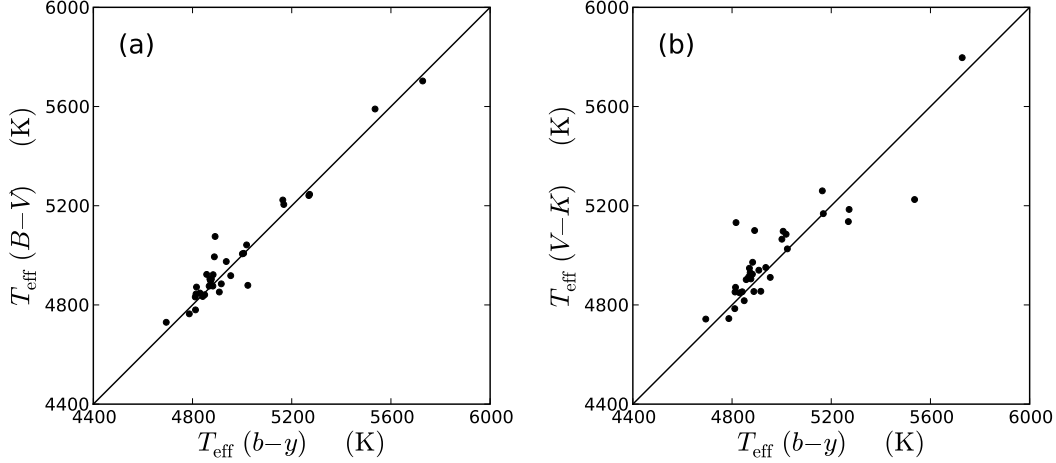


Fig. 1. Comparison of effective temperatures derived from different colour indices. (a): T_{eff} derived from $B - V$ versus that from $b - y$. (b): T_{eff} derived from $V - K$ versus that from $b - y$.

3. Stellar parameters

3.1. Effective temperature

Based on the empirical calibration relations given by Alonso et al. (1999, 2001), the effective temperatures (T_{eff}) of our program stars are determined using the $B - V$, $V - K$, and $b - y$ photometric data. The $B - V$ colour indices in Johnson system are obtained by $B - V = 0.850(B_T - V_T)$, as described by Perryman et al. (1997), where B_T and V_T are Tycho magnitudes in *Hipparcos Catalogue* (ESA 1997). The K magnitudes in $V - K$ are obtained by converting the K_s magnitude in Two Micron All Sky Survey (2MASS) to K magnitude using the calibration relation given by Ramírez & Meléndez (2004), and V magnitudes are taken from *Hipparcos Catalogue*. There are 32 stars of our sample also have $b - y$ data in catalogue given by Hauck & Mermilliod (1998). As a result, we derive the T_{eff} from $b - y$ besides $V - K$ and $B - V$, and compare the results with those from $B - V$ and $V - K$ in figure 1.

The color excess $E(B - V)_A$ is calculated according to Schlegel et al. (1998), with a slightly revision described by Arce & Goodman (1999) for those values larger than 0.15 mag. Then, the $E(B - V)$ value for each star is calculated as

$$E(B - V) = [1 - \exp(-|D \sin b|/125)]E(B - V)_A$$

where D is the distance of the star and b is the galactic latitude. Finally, we adopt $E(V - K) = 2.948E(B - V)$ as colour excess for $V - K$ (Schlegel et al. 1998), and $E(b - y) = 0.741E(B - V)$ for $b - y$ (Crawford et al. 1976).

The mean difference $\langle T_{\text{eff}}(B - V) - T_{\text{eff}}(b - y) \rangle$ is 16 ± 56 K, while the mean difference $\langle T_{\text{eff}}(V - K) - T_{\text{eff}}(b - y) \rangle$ is 24 ± 100 K. According to Alonso et al. (1999), the uncertainty of the effective temperature of giants derived from $V - K$ is estimated to be ± 40 K, which is

more accurate than that is derived from either $B - V$ ($\pm 96\text{K}$) or $b - y$ ($\pm 70\text{K}$). However, most stars in our sample are too bright in K_s band ($< 4^{\text{m}}.5$) to get accurate photometry, therefore the effective temperatures derived from $V - K$ may not be reliable. Table 1 list the effective temperatures derived from three different colour indices for the 32 stars.

Table 1. Comparison of effective temperatures derived from three different colour indices.

HD	T_{eff}^{b-y}	T_{eff}^{B-V}	T_{eff}^{V-K}	HD	T_{eff}^{b-y}	T_{eff}^{B-V}	T_{eff}^{V-K}	HD	T_{eff}^{b-y}	T_{eff}^{B-V}	T_{eff}^{V-K}
101853	4841	4834	4853	120651	4916	4885	4855	159797	4811	4832	4785
103690	4694	4730	4743	121303	4888	4994	4854	160823	4891	5076	5100
105475	4787	4764	4745	121883	4876	4904	4905	161502	4936	4975	4951
109545	5001	5006	5065	125113	4873	4896	4930	174621	5168	5205	5168
109894	4830	4848	4849	137463	5536	5590	5225	176973	4812	4780	4852
111381	4867	4876	4913	138425	5023	4879	5026	181878	5164	5223	5260
113021	4814	4844	4871	149522	4883	4922	4972	183585	5272	5246	5185
114877	4882	4876	4924	151879	5018	5042	5085	188993	5728	5703	5797
114988	5269	5241	5136	155231	4857	4923	4902	194579	5006	5008	5097
117877	4908	4852	4940	157261	4954	4918	4911	195194	4870	4904	4948
118670	4849	4841	4817	159466	4816	4872	5132				

Another method is the so-called “excitation equilibrium method”, which forces the derived iron abundances given by different FeI lines to be independent from their excitation potentials of lower states (χ_{low}). After adjusting effective temperatures, the slopes on $\log A - \chi_{\text{low}}$ diagrams for all stars in our sample are smaller than 0.002 dex/eV , and the mean difference $\langle T_{\text{eff}}(\text{eq}) - T_{\text{eff}}(B - V) \rangle$ is $44 \pm 117\text{K}$. The effective temperatures derived from this method and those from $B - V$ are compared in figure 2.

3.2. Surface gravity

Surface gravity ($\log g$) is determined by

$$\log g = \log g_{\odot} + \log \left(\frac{M}{M_{\odot}} \right) + 4 \log \left(\frac{T_{\text{eff}}}{T_{\text{eff},\odot}} \right) + 0.4(M_{\text{bol}} - M_{\text{bol},\odot}) \quad (1)$$

where M is the stellar mass, and M_{bol} is the bolometric magnitude defined as

$$M_{\text{bol}} = V_{\text{mag}} + BC - 5 \log d + 5 - A_V \quad (2)$$

where V_{mag} , BC , d , and A_V represent the apparent magnitude, bolometric correction, distance, and interstellar extinction, respectively.

The bolometric corrections (BC) are calculated based on estimated effective temperatures and metallicities, as given in Alonso et al. (1999). The stellar mass is estimated by an interpolation of Yale-Yonsei stellar evolution tracks (Demarque et al. 2004, Yi et al. 2003) which is based on a new convective core overshoot scheme. Yale-Yonsei evolution tracks can be used

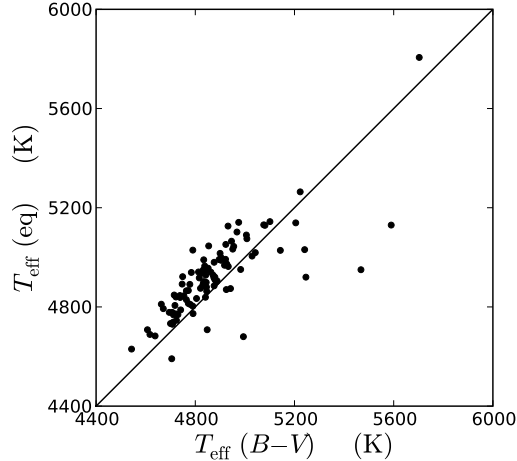


Fig. 2. Comparison of effective temperatures derived from $B - V$ and excitation equilibrium methods.

for stars from the stage of the pre-main-sequence to the helium-core flash. For comparison, we also estimated the masses using the evolution tracks of Girardi et al. (2000), in which the helium-core ignition phase is included. By assuming all the stars are corresponding to the post-RGB phase, we find the difference between the two sets of stellar mass is less than $0.3 M_{\odot}$. While about half of our program stars present an uncertainty of parallax up to 15%. According to equation (1) and (2), this will cause the error of ~ 0.13 dex in $\log g$, and about a factor of 1.3 in stellar mass. The interstellar extinctions are adopted by $A_v = 3.1E(B - V)$, and *Hipparcos* parallaxes are used to determine the absolute magnitudes (M_V).

We also adopt another method which is independent from parallax data to determine the surface gravities. As the FeII lines are more sensitive to surface gravities in cool stars than FeI lines, $\log g$ can be determined by forcing the abundances of FeII lines to be the same value as those given by FeI lines. Despite several uncertainties such as non-local thermodynamic equilibrium (NLTE) effects and very few Fe II lines, it is still meaningful to compare different sets of $\log g$ values. As shown in figure 3, the scatter tends to increase with decreasing surface gravities.

3.3. Atomic data

The $\log gf$ values for selected spectral lines are taken from various literatures, and listed in table 2. For Fe I lines, we use Oxford oscillator strength data (Blackwell 1982a,b, 1986). For the four heavy elements (Y, Ba, La, Eu), the $\log gf$ values are taken from Hannaford (1982), Weise & Martin (1980), Luck & Bond (1992), and Biemont et al. (1982), respectively. For other elements, we use the $\log gf$ values given by Chen et al. (2000). Although the atomic data are compiled from different references, it does not affect the results systematically. Moreover, the same program and values of oscillator strength are also adopted by measuring the EWs in

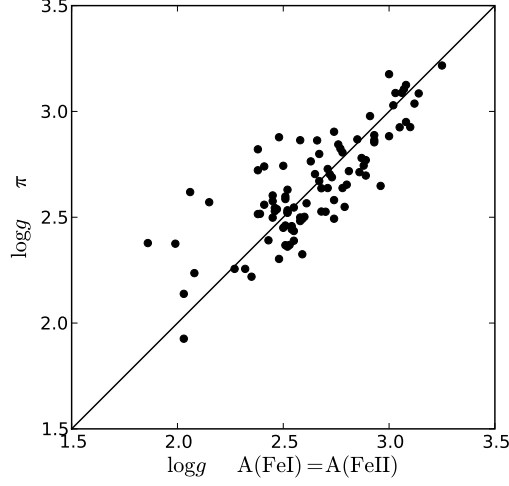


Fig. 3. Comparison of surface gravities obtained by *Hipparcos* parallaxes (Y axis) and ionization balance of FeI and FeII lines (X axis).

Solar Atlas (Kurucz et al. 1984) to determine the solar abundances, so the final results are the differential values relative to the Sun.

Table 2. Atomic line data.

λ_{air} (Å)	Element	χ_{low}	$\log gf$	E_{γ}
6327.604	Ni I	1.68	-3.150	2.5
6335.337	Fe I	2.20	-2.177	1.2
6336.830	Fe I	3.69	-0.856	1.4
6344.155	Fe I	2.43	-2.923	1.3
...

3.4. Metallicity and microturbulence velocity

For most of our program stars, the initial metallicity values are set to $[\text{Fe}/\text{H}]=0.0$. For those stars that have been studied, the initial values are taken from previous literatures (da Silva et al. 2006, Mishenina et al. 2006, Luck & Heiter 2007, and Tekeda et al. 2008). The abundances of chemical elements are determined based on the model atmospheres interpolated by a plane-parallel, homogeneous and local thermodynamic equilibrium (LTE) model grid by Kurucz (1993). Chemical abundances are calculated with ABONTEST8 program supplied by Dr. P. Magain (Liege, Belgium). It calculates the theoretical equivalent widths from the atmospheric model, and matches them with observed values. Several broadening mechanism have been taken into account, including natural broadening, thermal broadening, van der Waals damping broadening, and microturbulent broadening. The microturbulence ξ_t is determined by forcing the iron abundance values given by different Fe I lines to be independent from their

EWs and hence with zero slope on $\log A$ - EW diagram. Only those Fe I lines with $10 \text{ m}\text{\AA} < EW < 110 \text{ m}\text{\AA}$ are used.

3.5. Summary

The derived physical parameters of our program stars are summarized in table 3 and 4. In table 3, effective temperatures are derived from $B - V$ and surface gravities are derived from *Hipparcos* parallaxes. While in table 4, effective temperatures and surface gravities are derived from excitation equilibrium and ionization balance, respectively. Although two different sets of stellar parameters are given, we finally adopt those listed in table 3 in the following analysis.

Table 3. Physical parameters of program stars. Effective temperatures are derived from $B - V$ and calibration relation of Alonso et al. (1999). Surface gravities are derived from *Hipparcos* parallaxes.

HD	T_{eff} (K)	[Fe/H]	$\log g$	$\xi_t (\text{kms}^{-1})$	$B - V$	$E(B - V)$	M_v	BC	M/M_\odot	$\log age$	$\log(L/L_\odot)$
100055	4900	-0.16	2.780	1.79	0.929	0.008	0.720	-0.296	2.29	8.90	1.77
101853	4834	-0.21	2.549	1.76	0.955	0.019	0.098	-0.322	2.58	8.75	2.00
103690	4730	-0.32	2.499	1.61	0.996	0.010	0.560	-0.366	1.70	9.24	1.84
105475	4764	-0.10	2.638	1.46	1.007	0.016	0.345	-0.351	2.74	8.69	1.94
...

Table 4. Atmospheric parameters of program stars. Effective temperatures are derived from excitation equilibrium method. Surface gravities are derived from ionization balance method.

HD	T_{eff} (K)	[Fe/H]	$\log g$	$\xi_t (\text{kms}^{-1})$
100055	5016	-0.07	2.87	1.76
101853	4990	-0.09	2.79	1.76
103690	4769	-0.29	2.58	1.60
105475	4865	-0.03	2.71	1.44
...

In figure 4 $\log(L/L_\odot)$ versus T_{eff} is plotted for our program stars. It is shown that most of our samples have luminosities $1.5 < \log L/L_\odot < 2.0$, and effective temperatures $3.67 < \log T/T_{\text{eff}} < 3.70$. In figure 5, the derived atmospheric parameters of our stars (filled circles) are compared with those derived by Takeda et al. (2008) (open circles) and Liu et al. (2010) (crosses). The effective temperature (T_{eff}) tends to increase with increasing surface gravity ($\log g$), and the microturbulent velocity (ξ_t) tends to decrease with higher surface gravity ($\log g$).

3.6. Consistency check with literatures

In order to check the consistency of our atmospheric parameters with previous studies, the results are compared with those given by da Silva et al. (2006), Mishenina et al. (2006),

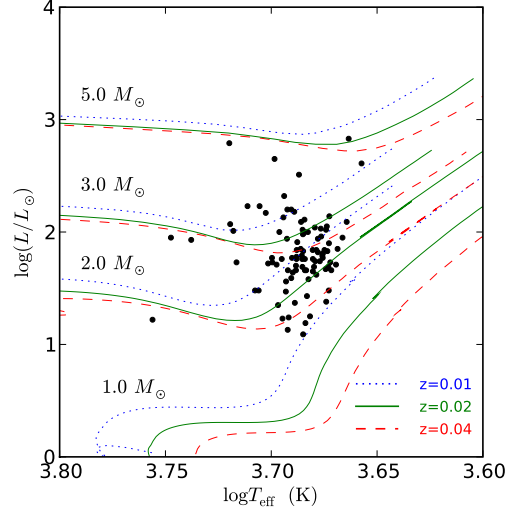


Fig. 4. Luminosity versus effective temperature of our program stars, together with the Yale-Yonsei evolution tracks (Demarque et al. 2004) of stars with different masses ($1 M_{\odot}$, $2 M_{\odot}$, $3 M_{\odot}$, and $5 M_{\odot}$) and metallicity ($z=0.04$, 0.02 , and 0.01 , corresponding to $[\text{Fe}/\text{H}] = +0.3$, 0.0 , and -0.3 , respectively).

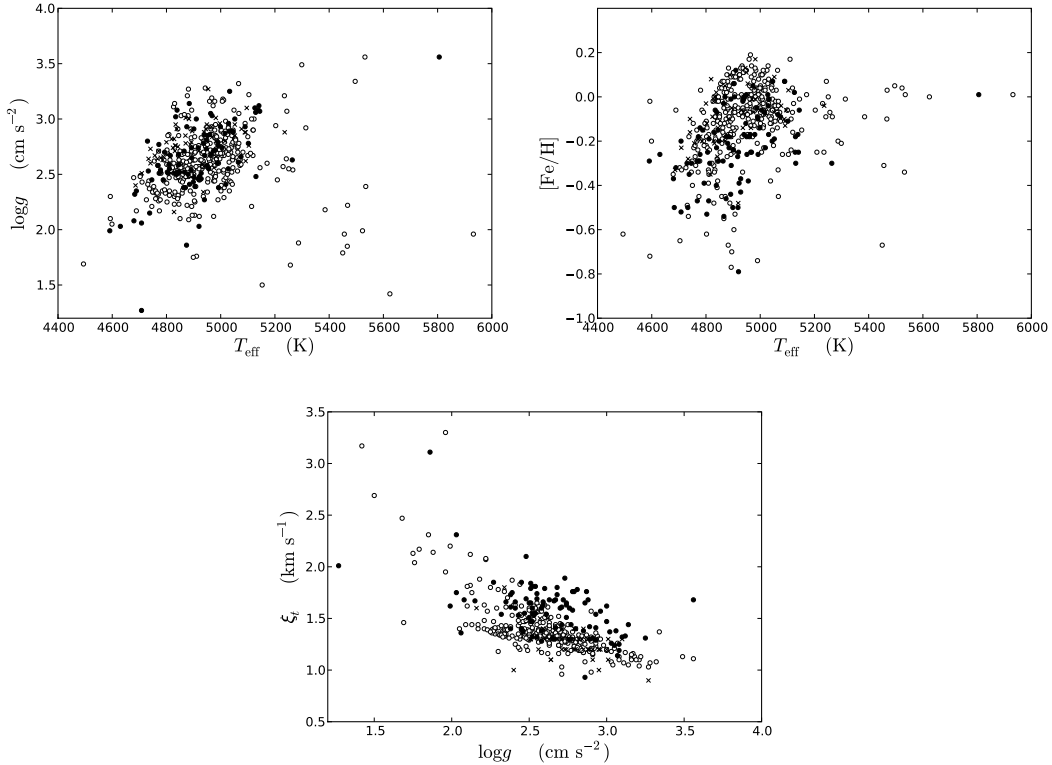


Fig. 5. Relations of atmospheric parameters ($\log g$ vs. T_{eff} , $[\text{Fe}/\text{H}]$ vs. T_{eff} , ξ_t vs. $\log g$) derived from $B - V$. Filled circles: this study, open circles: Tekeda et al. (2008), and crosses: Liu et al. (2010).

Hekker & Melendez (2007), Luck & Heiter (2007), Tekeda et al. (2008), and Sato et al. (2010). All literatures above have determined the parameters of giants based on high resolution spectra. There are totally 7 common stars in our sample with those literatures, as listed in table 5. Figure 6 compares the effective temperatures, surface gravities, and metallicity of these stars. Our derived temperatures are well consistent with others, with $\Delta T_{\text{eff}} \sim 4 \pm 65 \text{ K}$ lower than their values. While the surface gravity difference $\Delta \log g$ is $\sim 0.14 \pm 0.33$ dex lower compared with others' results, and the metallicity difference $\Delta [\text{Fe}/\text{H}]$ is $\sim 0.09 \pm 0.07$ dex lower than those from literatures.

Table 5. Common stars in this study and other literatures

HD	Literature
145457	Sato et al. 2010
161502	Luck & Heiter 2007
179799	da Silva et al. 2006
180314	Sato et al. 2010
185351	Tekeda et al. 2008
	Hekker & Melendez 2007
188993	Luck & Heiter 2007
196134	Mishenina et al. 2006

4. Chemical abundances

We use the atmospheric parameters listed in table 3 to derive the $[\text{X}/\text{Fe}]$ ratios of 14 elements (Al, Ba, Ca, Cr, Eu, K, La, Mg, Ni, Sc, Si, Ti, V and Y). Those trends are plotted in figure 9 to figure 13 (filled circles), together with the trends from Takeda et al. (2008, open circles) as a comparison. The measured equivalent widths of the selected lines of our program stars are listed in table 9, which is only available in the electronic form.

4.1. Error analysis

The uncertainties of chemical abundances are estimated by changing the atmospheric parameters in a reasonable range. Table 6 shows the abundances differences due to deviations of the effective temperature of 100 K, the surface gravity of 0.15 dex, the iron abundance of 0.1 dex, and the microturbulent velocity of 0.1 km s^{-1} . For most of the chemical elements, the uncertainties are less than 0.1 dex, except of Ti and V. The uncertainties of these two elements can be as high as 0.15 dex.

Another source of uncertainties is the error of equivalent widths caused by mixture of the intrinsic stellar lines and the I_2 lines, since the spectra of our program stars are I_2 -superposed for precise radial velocity measurements. To check the uncertainties caused by iodine lines, we use the pure stellar spectra of HD 145457 taken in OAO to measure the equivalent widths, and

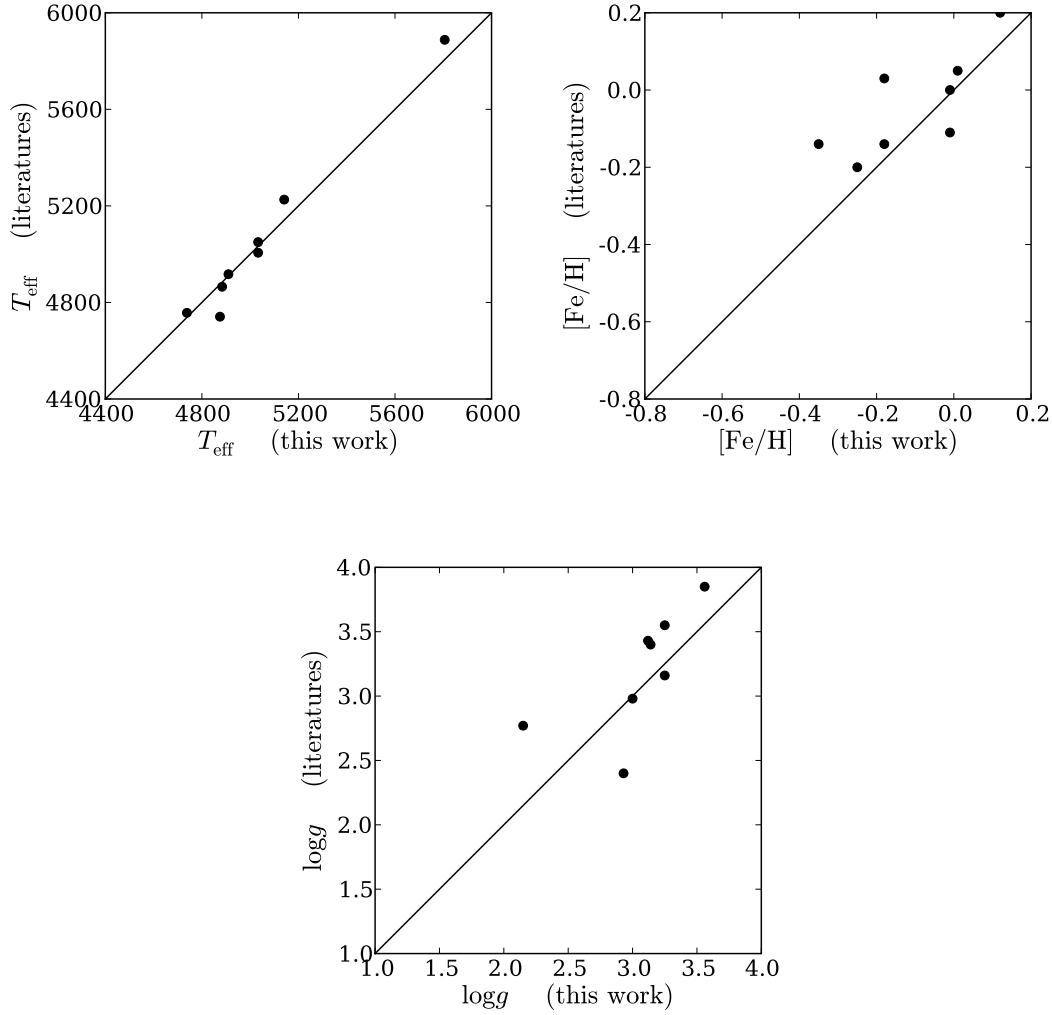


Fig. 6. Comparison of atmospheric parameters of common stars in this study and other literatures. Upper panel: effective temperature, middle panel: metallicity, bottom panel: surface gravity.

determine the chemical abundances.

In Doppler surveys, spectra of fast-rotation B type stars are often obtained with I_2 cell to deconvolute instrumental profiles (IPs, e.g. Butler et al. 1996). The spectra of such stars are featureless, and thus provide a simple way to check how the stellar spectra are contaminated by I_2 absorption lines at different wavelengths in this study. The I_2 -superposed spectra of a B star (HR 5685, B8V), I_2 -superposed spectra of HD 145457, and the pure spectra of HD 145457 around 6400 Å and 6700 Å are plotted in figure 7. Around 6400 Å, the integrated equivalent width of I_2 lines is about 6 mÅ/Å, which causes the uncertainty of equivalent width of about 3 ~ 4 mÅ for a typical spectral line in our I_2 -superposed spectrum in this region. While around 6700 Å, the integrated equivalent width of I_2 lines is about 4 mÅ/Å, 30% smaller than that around 6400 Å. The uncertainty of equivalent width caused by I_2 lines is estimated to be 2 mÅ.

Table 6. Estimated errors for abundances of a typical late-type giant HD109305, with $T_{\text{eff}} = 4663$ K, $\log g = 2.44$, $[\text{Fe}/\text{H}] = -0.30$, and $\xi_t = 1.77 \text{ km s}^{-1}$, taken from table 3.

$\Delta[\text{X}/\text{H}]$	ΔT_{eff} (+100K)	$\Delta \log g$ (+0.15)	$\Delta[\text{Fe}/\text{H}]$ (+0.1)	$\Delta \xi_t$ (+0.1 km s^{-1})	σ_{Total}
$\Delta[\text{FeI}/\text{H}]$	0.06	0.01	0.01	-0.02	0.06
$\Delta[\text{FeII}/\text{H}]$	-0.07	0.08	0.04	-0.02	0.12
$\Delta[\text{Mg}/\text{H}]$	0.05	-0.01	0.01	-0.01	0.05
$\Delta[\text{Al}/\text{H}]$	0.07	-0.01	0.00	-0.02	0.07
$\Delta[\text{Si}/\text{H}]$	-0.02	0.03	0.02	-0.01	0.04
$\Delta[\text{Ca}/\text{H}]$	0.10	-0.01	0.00	-0.04	0.11
$\Delta[\text{Sc}/\text{H}]$	-0.01	0.06	0.03	-0.03	0.07
$\Delta[\text{Ti}/\text{H}]$	0.15	0.00	-0.01	-0.03	0.15
$\Delta[\text{V}/\text{H}]$	0.15	0.00	0.00	-0.01	0.15
$\Delta[\text{Cr}/\text{H}]$	0.09	0.00	0.00	-0.03	0.09
$\Delta[\text{Ni}/\text{H}]$	0.05	0.03	0.02	-0.02	0.06
$\Delta[\text{Y}/\text{H}]$	-0.01	0.07	0.04	0.00	0.08
$\Delta[\text{Ba}/\text{H}]$	0.02	0.02	0.06	-0.05	0.08
$\Delta[\text{La}/\text{H}]$	0.02	0.07	0.04	-0.01	0.08
$\Delta[\text{Eu}/\text{H}]$	-0.01	0.07	0.04	-0.01	0.08
$\Delta[\text{K}/\text{H}]$	0.10	-0.04	0.01	-0.05	0.12

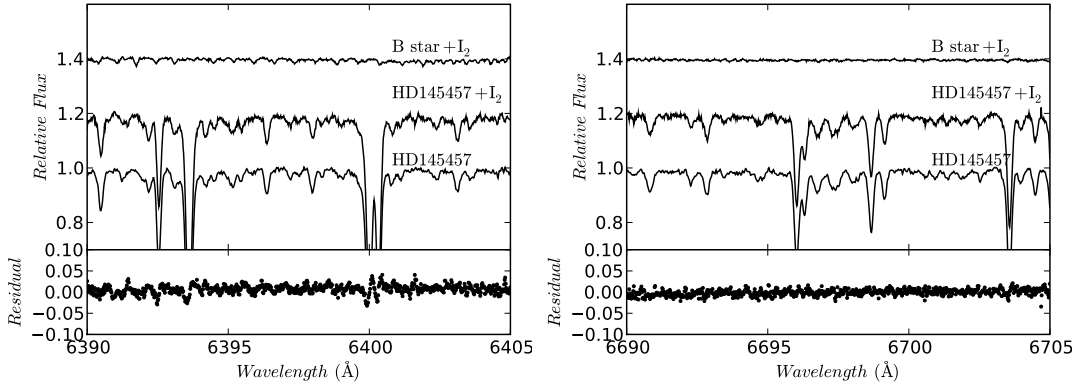


Fig. 7. Comparison of the I_2 -superposed spectrum (taken in Subaru) and the pure spectrum (taken in OAO) for HD 145457 around 6400 \AA and 6700 \AA . The calculated RMS residuals are 1.2% around 6400 \AA and 0.7% around 6700 \AA . Two portions of I_2 -superposed spectrum for a fast rotation, B-type star (HR 5685, taken in Subaru) are also plotted in the upper panel.

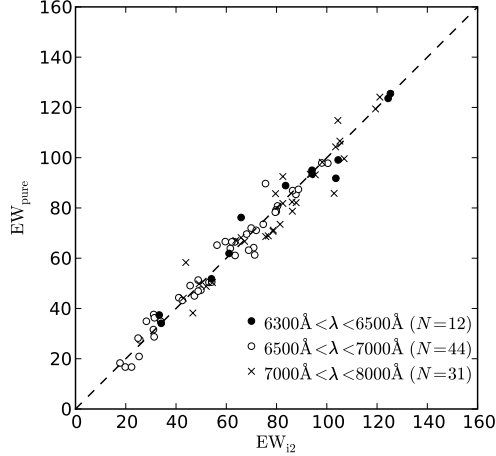


Fig. 8. Comparison of equivalent widths (EWs) measured using I_2 -superposed spectra taken in Subaru (X axis) and pure spectra taken in OAO (Y axis). The spectral lines are separated into three groups according to their wavelengths. The filled circles are 12 lines with wavelengths $\lambda < 6500 \text{ \AA}$. The open circles are 44 lines with wavelengths $6500 \text{ \AA} < \lambda < 7000 \text{ \AA}$. The crosses are 31 lines with wavelengths $\lambda > 7000 \text{ \AA}$. The mean differences $\langle EW_{I_2} - EW_{\text{pure}} \rangle$ are $-0.05 \pm 5.22 \text{ m\AA}$, $-0.33 \pm 4.33 \text{ m\AA}$, and $+1.48 \pm 6.38 \text{ m\AA}$, respectively.

Furthermore, we measure the equivalent widths using the I_2 -superposed spectrum and pure spectrum of HD 145457. The spectral lines are separated into three groups, with wavelengths $\lambda < 6500 \text{ \AA}$, $6500 \text{ \AA} < \lambda < 7000 \text{ \AA}$, and $\lambda > 7000 \text{ \AA}$, respectively. The results are compared in figure 8. We find that the mean differences $\langle EW_{I_2} - EW_{\text{pure}} \rangle$ of three groups are $-0.05 \pm 5.22 \text{ m\AA}$, $-0.33 \pm 4.33 \text{ m\AA}$, and $+1.48 \pm 6.38 \text{ m\AA}$, which infers our EW values are not significantly influenced by I_2 absorption lines. The chemical abundances determined by pure stellar spectra are compared with our results using Subaru spectra in table 7. It is shown that the uncertainties of chemical abundances caused by mixture of I_2 lines are range from $0.02 \sim 0.09 \text{ dex}$, which are smaller than the uncertainties caused by errors of atmospheric parameters. Therefore, we concluded that the weak I_2 absorption lines in the red part of our spectra nearly do not affect the chemical abundances measurements.

4.2. α -elements (*Mg, Si, Ca, Ti*)

The α elements are mainly produced in SNe II nucleosynthesis (Woosley & Weaver 1995) and show enhancement in metal-poor stars. In figure 9, we plot $[X/\text{Fe}]$ ratios of Mg, Si, Ca, and Ti I versus $[\text{Fe}/\text{H}]$, together with the trends take from Takeda et al. (2008). Except for the trend of $[\text{TiI}/\text{Fe}]$ versus $[\text{Fe}/\text{H}]$ with a large scatter, three of the other α elements exhibit enhancement towards lower metallicity. However, their decreasing trends with increasing metallicity are slightly different. Both the $[\text{Mg}/\text{Fe}]$ and $[\text{Ca}/\text{Fe}]$ show a turn off trend towards a flat pattern at $[\text{Fe}/\text{H}] \sim -0.2$, which is in good agreement with previous studies on both giants (Takeda et al. 2008, Liu et al. 2007) and dwarfs (Chen et al. 2000), while the $[\text{Mg}/\text{Fe}]$ turns to decrease at

Table 7. Comparison of chemical abundances of HD 145457 determined by pure stellar spectra taken in OAO, and I₂ superposed spectra taken in Subaru.

$\Delta[X/H]$	$[X/H]_{i2} - [X/H]_{\text{pure}}$
$\Delta[\text{FeI}/H]$	0.02
$\Delta[\text{FeII}/H]$	0.04
$\Delta[\text{Mg}/H]$	0.04
$\Delta[\text{Al}/H]$	0.03
$\Delta[\text{Si}/H]$	0.04
$\Delta[\text{Ca}/H]$	0.09
$\Delta[\text{Sc}/H]$	0.06
$\Delta[\text{Ti}/H]$	0.04
$\Delta[\text{V}/H]$	0.02
$\Delta[\text{Cr}/H]$	0.07
$\Delta[\text{Ni}/H]$	0.07
$\Delta[\text{Y}/H]$	0.02
$\Delta[\text{Ba}/H]$	0.02
$\Delta[\text{La}/H]$	0.03
$\Delta[\text{Eu}/H]$	0.02
$\Delta[\text{K}/H]$	—

$[\text{Fe}/H] > 0$. Despite an increasing trend with decreasing metallicity for $[\text{Fe}/H] < -0.4$, $[\text{Si}/\text{Fe}]$ shows a larger scatter for higher metallicity, leaving the flat pattern shown in Tekeda et al. (2008) (open circles in figure 9) unclear. Oxygen is another important α element for giants. But in our spectra, the $[\text{O I}]$ forbidden lines at 6300 Å are not covered by the CCD, and the lines at 6363 Å are very weak and closed to the edge. To make sure our results are reliable, the oxygen abundance is not included in this study.

4.3. Odd-Z light elements (*Al, K, Sc*)

As shown in figure 10, $[\text{Al}/\text{Fe}]$ shows a decreasing trend with increasing metallicity for $[\text{Fe}/H] < -0.2$, and a solar pattern towards higher metallicity. Our results are consistent with Liu et al. (2007). Chen et al. (2000) found a rather steep upturn of $[\text{Al}/\text{Fe}]$ at $[\text{Fe}/H] = -0.2$ in a sample of dwarfs. However, in our results the upturn is rather smooth. $[\text{K}/\text{Fe}]$ exhibits a larger dispersion, because only very few number of lines are available. The trend of $[\text{Sc}/\text{Fe}]$ is similar with that of $[\text{Ti}/\text{Fe}]$, with both of them showing a flat pattern when data with larger dispersion are excluded. This result is also consistent with Tekeda et al. (2008).

4.4. Iron-peak elements (*V, Cr, Ni*)

The iron-peak elements are believed to be mainly produced in SNe Ia, and should have the same abundance patterns with iron. In figure 11, we plot $[X/\text{Fe}]$ versus $[\text{Fe}/H]$ for three iron-

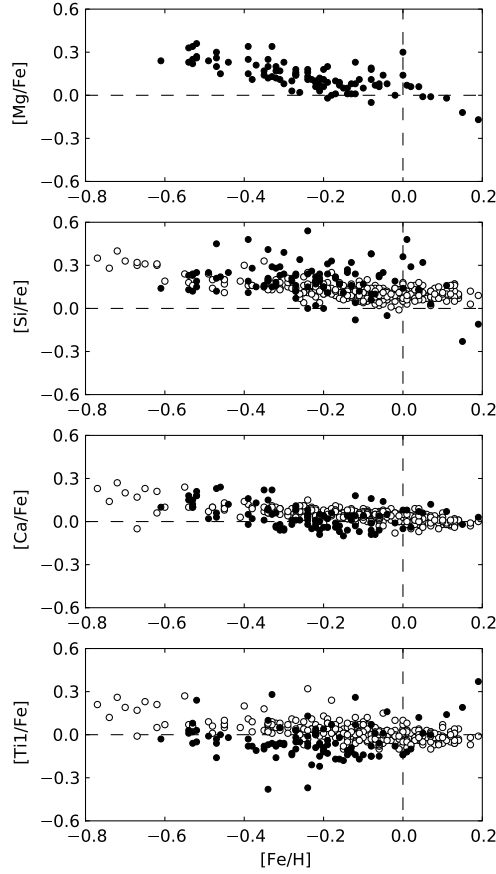


Fig. 9. Abundance ratio $[X/\text{Fe}]$ for four α elements (Mg, Si, Ca, and Ti I) against $[\text{Fe}/\text{H}]$ (filled circles), together with the results from Takeda et al. (2008, open circles).

peak elements (V, Cr, and Ni). $[\text{V}/\text{Fe}]$ shows an increasing trend with increasing metallicity, which is contrast to Takeda’s results (plotted as open circles in the same figure). The hyper fine structure (HFS) effect has been considered in our work. The adopted HFS data is taken from Kurucz³. Liu et al. (2007) suggests the HFS effect can lead to a correction as large as 0.5 dex for vanadium abundance in giants. However, we find that the corrections due to introduction of HFS effect are between -0.002 dex and 0.012 dex, and can be neglected (see figure 12). The discrepancy is due to the difference of HFS effect from line to line, and the vandium lines we used in this work are different from those in Liu et al. (2007).

The $[\text{Cr}/\text{Fe}]$ trend in our sample is consistent with Takeda’s, except for a few stars with higher $[\text{Cr}/\text{Fe}]$ values. For these stars, the relation of $[\text{Ni}/\text{Fe}]$ vs. $[\text{Fe}/\text{H}]$ keeps the solar pattern in the range of $-0.8 < [\text{Fe}/\text{H}] < -0.1$, while shows overabundance for higher metallicity and hence systematically higher than Takeda’s result. The possible upturn at $[\text{Fe}/\text{H}] \sim 0.0$ has also been found in giants (e.g. Liu et al. (2007)) and dwarfs (e.g. Edvardsson et al. 1993).

³ <http://kurucz.harvard.edu/linelists.html>

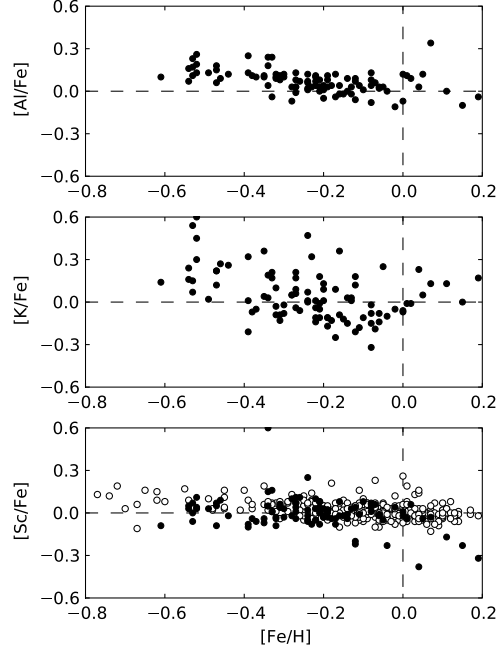


Fig. 10. Abundance trends of $[X/Fe]$ against $[Fe/H]$ for three odd- z elements (Al, K, and Sc, filled circles). Results of $[Sc/Fe]$ from Takeda et al. (2008) are plotted as open circles.

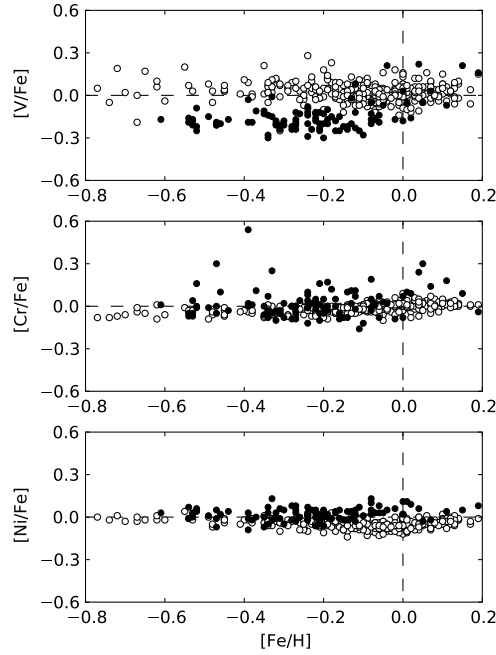


Fig. 11. Abundance trends of $[X/Fe]$ against $[Fe/H]$ for three iron-peak elements (V, Cr, and Ni, filled circles). Results from Takeda et al. (2008) are plotted as open circles.

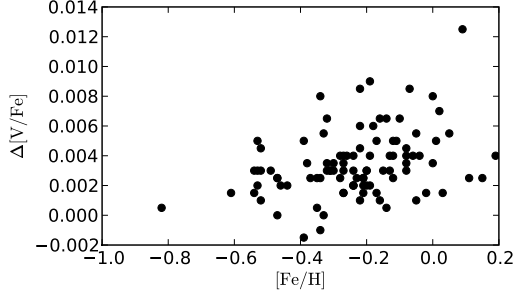


Fig. 12. The difference in vanadium abundances obtained by neglecting HFS minus those by considering HFS versus $[\text{Fe}/\text{H}]$. $\Delta[\text{V}/\text{Fe}]$ on Y axis represents $\log V_{\text{non-HFS}} - \log V_{\text{HFS}}$.

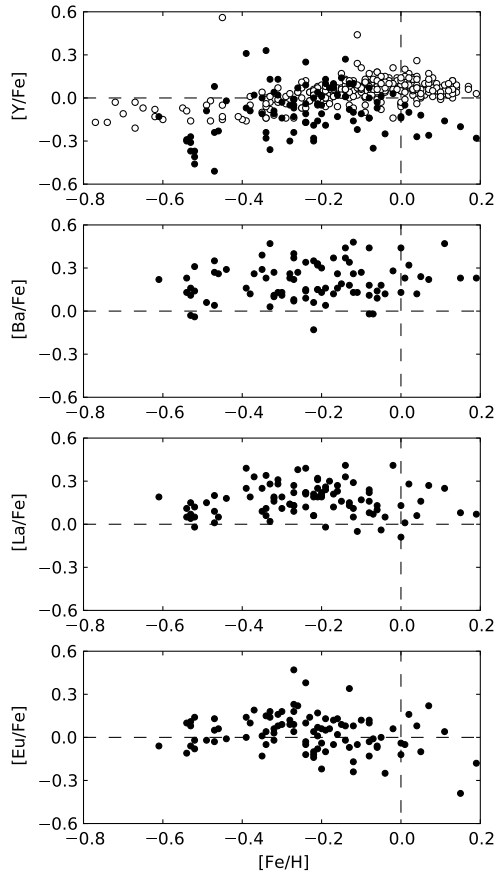


Fig. 13. Abundance trends of $[\text{X}/\text{Fe}]$ against $[\text{Fe}/\text{H}]$ for four heavy elements (Y, Ba, La, and Eu). (filled circles: this work; open circles: Takeda et al. 2008's work)

4.5. Heavy elements (*Y, Ba, La, Eu*)

Those elements heavier than iron are mainly produced via the neutron capture process. Two major mechanisms are generally considered: the r-process and s-process, corresponding to neutron rich and neutron poor environment, respectively. In our analysis, one r-process element

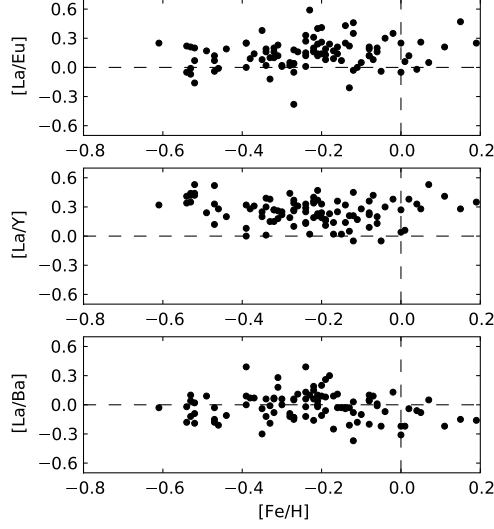


Fig. 14. [La/Eu], [La/Y], [La/Ba] as a function of [Fe/H] (from top to bottom).

(Eu), one light s-process element (Y) and two heavy s-process elements (Ba, La) are included. Their abundances trend against [Fe/H] are plotted in figure 13.

Despite a large scatter as often observed in field stars, the ratio of [La/Eu], [La/Y], and [La/Ba] may provide important information of the Galactic chemical evolution history. As a typical r-process element, europium is mainly produced in core-collapse supernovae (SNe) with masses $8 M_{\odot} < M < 10 M_{\odot}$ and the pattern still remains uncertain. Previous work (Simmerer et al. 2004) of La and Eu revealed the s-process may be active as early as $[\text{Fe}/\text{H}] = -2.6$. In figure 14, [La/Eu], [La/Y], and [La/Ba] are plotted as functions of [Fe/H] (from top to bottom). From our plot, a decline of [La/Eu], although not very clearly, can be seen in lower metallicity down to -0.7. In the convection zone of low mass AGB stars where the slow neutron capture reactions take place, the neutron flux per seed nuclei is inversely proportional to the density of iron-peak nucleus. The metal-poor stars produce light s-process elements (such as Y) more efficiently than the heavy s-process elements (such as Ba, La). The [La/Y] versus [Fe/H] in the middle panel of figure 14 shows an marginal increasing trend with decreasing metallicity, consistent with the theoretical prediction (e.g. Busso et al. 1999). [La/Ba] shows a flat trend with [Fe/H] in the bottom panel of figure 14. This is consistent with the theoretical prediction that they are produced through the same producing mechanism.

5. Kinetics Parameters

We derived the kinetics parameters (U_{LSR} , V_{LSR} , W_{LSR}) based on the method given by Johnson & Soderblom (1987). The radial velocities (RV_{helio}) are measured based on our spectra, and corrected to heliocentric velocities. Positions, parallaxes, and proper motions are taken from *Hipparcos* data. By adopting a solar motion of $(U, V, W)_{\odot} = (-10.00 \pm 0.36, +5.25 \pm$

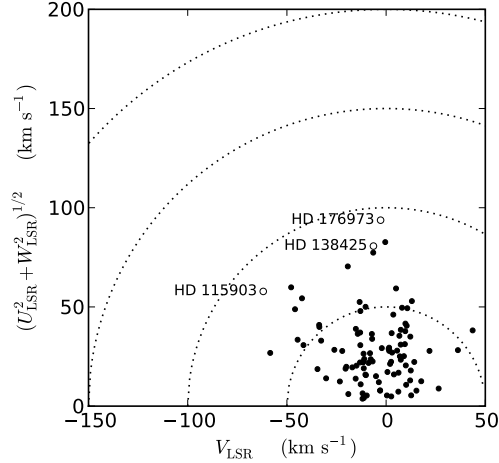


Fig. 15. Toomre diagram of program stars. Thin disk stars ($TD/D < 1.0$) and thick disk stars ($TD/D > 1.0$) are plotted as filled and open circles, respectively (See discussion in Sect. 5). Dotted lines indicate constant total velocities $|v|_{\text{LSR}} = \sqrt{U_{\text{LSR}}^2 + V_{\text{LSR}}^2 + W_{\text{LSR}}^2}$ in steps of 50 km s^{-1} .

$0.62, +7.17 \pm 0.38$) ⁴ in kms^{-1} , given by Dehnen & Binney (1998), the Galactic velocity components U , V , and W of our program stars are corrected to local standard of rest (LSR). It is hard to clarify whether a star in solar neighborhood belongs to the thin disk or the thick disk. We apply the kinematic method proposed by Bensby et al. (2003) to calculate the relative probability for the thick-disk-to-thin-disk (TD/D) membership. In Bensby et al. (2003), thin disk and thick disk stars are thought to follow Gaussian distributions in Galactic velocity space (U , V , W). By assuming different asymmetric velocity drifts and dispersions, the relative probability of belonging to different populations can be calculated. For instance, a star with $TD/D = 10$ means it is 10 times more likely to belong to the thick disk than to the thin disk. In our sample, one star (HD 115903) with $TD/D > 10.0$ and two stars (HD 138425 and HD 176973) with $1.0 < TD/D < 10.0$ are more likely to be a thick disk star rather than a thin disk star. Those stars are plotted as open circles on Toomre diagram in figure 15, and listed with a mark ‘TD’ in the last column of table 8, as well as their kinetics parameters mentioned above.

6. Conclusion

In this work we determine the atmospheric parameters, kinematic properties and chemical abundances of 99 late-type giants based on high resolution spectra obtained in Subaru Planet Search Program, covering the metallicity range $-0.8 < [\text{Fe}/\text{H}] < +0.2$. We get two sets of stellar parameters derived from different methods. The photospheric chemical abundances of 15 elements, including four α -elements (Mg, Si, Ca, Ti), three odd- Z light elements (Al, K,

⁴ In this work the Galactic velocity component U is defined to be positive towards Galactic anticenter.

Table 8. Kinetics parameters of program stars

HD	RV_{helio} (kms^{-1})	U_{LSR} (kms^{-1})	V_{LSR} (kms^{-1})	W_{LSR} (kms^{-1})	TD/D
100055	6.69 ± 0.37	2.9 ± 1.3	-15.4 ± 2.6	13.5 ± 0.7	0.01
101853	2.81 ± 0.36	-30.9 ± 3.4	6.7 ± 0.7	17.3 ± 1.3	0.01
103690	-19.28 ± 0.35	-58.6 ± 3.8	5.0 ± 1.1	8.9 ± 1.7	0.02
105475	0.35 ± 0.35	-80.9 ± 11.8	-0.4 ± 1.3	16.9 ± 1.7	0.06
...

Sc), four iron peak elements (V, Cr, Fe, Ni), and four neutron-capture elements (Y, Ba, La, Eu) are determined. The kinematic parameters are calculated, and most of our sample are thin disk stars. From the results of abundances, we conclude that the abundance ratios $[\text{Mg}/\text{Fe}]$ and $[\text{Ca}/\text{Fe}]$ show an increasing trend with decreasing metallicity for $-0.8 < [\text{Fe}/\text{H}] \lesssim -0.2$, while flatten out towards higher metallicity. A decreasing trend of $[\text{Mg}/\text{Fe}]$ with increasing metallicity is detected for giants at $[\text{Fe}/\text{H}] > 0$. The upturn of $[\text{Al}/\text{Fe}]$ versus $[\text{Fe}/\text{H}]$ at $[\text{Fe}/\text{H}] = -0.2$ in giants is not as steep as that in dwarfs (e.g. Chen et al. 2000). The $[\text{Ni}/\text{Fe}]$ versus $[\text{Fe}/\text{H}]$ shows an upturn at $[\text{Fe}/\text{H}] = 0.0$ and an overabundance towards higher metallicity. The $[\text{La}/\text{Y}]$ ratio shows an increasing trend with decreasing metallicity, which is consistent with the prediction of AGB nucleosynthesis.

Acknowledgements

WL is grateful of Prof. Chen Yuqin and Dr. Li Haining for valuable comments and discussions. This work is supported by the National Natural Science Foundation of China under grant number 10821061 and 10803010.

References

- Alonso, A., Arribas, S., & Martínez-Roger, C., 1999, A&AS, 140, 261
Alonso, A., Arribas, S., & Martínez-Roger, C., 2001, A&AS, 376, 1039
Arce, H. G., & Goodman, A. A., 1999, ApJL, 512, L135
Bensby T., Feltzing S., Lundström I., 2003, A&A, 410, 527
Biemont, E., Karner, C., Meyer, G., Traeger, F., & Zu Putlitz, G., 1982, A&A, 107, 166
Blackwell, D. E., Petford, A. D., Shallis, M. J., & Simmons, G. J., 1982a, MNRAS, 43, 199
Blackwell, D. E., Petford, A. D., & Simmons, G. J., 1982b, MNRAS, 201, 595
Blackwell, D. E., Booth, A. J., Haddock, D. J., Petford, A. D., & Leggett, S. K., 1986, MNRAS, 220, 549
Busso, M., Gallino, R., & Wasserburg, G. J., 1999, ARA&A, 37, 239
Butler, R. P., Marcy, G. W., Williams, E., McCarthy, C., Dosanji, P., & Vogt, S. S. 1996, PASP, 108, 500

- Chen, Y. Q., Nissen, P. E., Zhao, G., Zhang, H. W., & Benoni, T., 2000, A&AS, 141, 491
- Chen, Y. Q., & Zhao, G., 2006, AJ, 131, 1816
- Crawford D. L. et al., 1976, PASP, 88, 917
- da Silva L. et al. 2006, A&A, 458, 609
- Dehnen W., & Binney J.J., 1998, MNRAS, 298, 387
- Demarque, P., Woo, J.-H., Kim, Y.-C., & Yi, S. K., 2004, ApJS, 155, 667
- Edvardsson, B., Andersen, J., Gustafsson, B., Lambert, D. L., Nissen, P. E., & Tomkin, J., 1993, A&A, 275, 101
- ESA, 1997, *The Hipparcos and Tycho Catalogues*, 1239
- Girardi, L., Bressan, A., Bertelli, G., Chiosi, C., 2000, A&AS, 141, 371
- Hannaford, P., Lowe, R. M., Grevesse, N., Biemont, E., & Whaling, W., 1982, ApJ, 261, 736
- Hauck, B., & Mermilliod, M., 1998, A&AS, 129, 431
- Hekker, S. & Meléndez, J., 2007, A&A, 475, 1003
- Ida, S., & Lin, D. N. C., 2004, ApJ, 604, 388
- Izumiura, H., 2005, JKAS, 38, 81
- Johnson D. R. H. & Soderblom D. R. 1987, AJ, 93, 864
- Kurucz, R. L., Furenlid, I., Brault, J., & Testerman, L., 1984, *Solar flux atlas from 296 to 1300 nm*
- Kurucz, R., 1993, *Kurucz CD-ROM No. 13. Cambridge, Mass.: Smithsonian Astrophysical Observatory*
- Liu, Y. J., Zhao, G., Shi, J. R., Pietrzyński, G., & Gieren, W., 2007, MNRAS, 382, 553
- Liu, Y., Sato, B., Takeda, Y., Ando, H., & Zhao, G., 2010, PASJ, 62, 1071
- Luck, R.E. & Bond, H. E., 1991, ApJS, 77, 515
- Luck, R.E. & Heiter, U., 2007, AJ, 133, 2464
- Mayor, M., & Queloz, D., 1995, Nature, 378, 355
- Mishenina T. V., Bienaym O., Gorbaneva T. I., Charbonnel C., Soubiran C., Korotin S. A., Kovtyukh V. V., 2006, A&A, 456, 1109
- Noguchi, K., et al., 2002, PASJ, 54, 855
- Perryman, M. & Flaherty, K. & van Leeuwen, F., 1997, ESA SP, 1200, 0
- Ramírez, I., & Meléndez, J., 2004, ApJ, 609, 417
- Santos, N. C. et al., 2004, A&A, 427, 1085
- Sato, B. et al., 2010, PASJ, 62, 1063
- Schlegel, D. J., & Finkbeiner, D. P., & Davis, M., 1998, ApJ, 500, 525
- Simmerer, J., Sneden, C., Cowan, J. J., Collier, J., Woolf, V. M., & Lawler, J. E., 2004, ApJ, 617, 1091
- Takeda, Y., 2007, PASJ, 59, 335
- Takeda, Y., Sato, B., & Murata, D., 2008, PASJ, 60, 781
- Weise, W. L., & Martin, G. A., 1980, NSDRS-NBS, 68
- Woosley, S. E., & Weaver, T. A., 1995, ApJS, 101, 181
- Yi, S. K., Kim, Y.-C., & Demarque, P., 2003, ApJS, 144, 259

